

# 1 Vertical structure of biomass burning aerosol transported over 2 the southeast Atlantic Ocean

3 Harshvardhan Harshvardhan<sup>1</sup>, Richard Ferrare<sup>2</sup>, Sharon Burton<sup>2</sup>, Johnathan Hair<sup>2</sup>, Chris  
4 Hostetler<sup>2</sup>, David Harper<sup>2</sup>, Anthony Cook<sup>2</sup>, Marta Fenn<sup>3</sup>, Amy Jo Scarino<sup>3</sup>, Eduard Chemyakin<sup>3</sup>,  
5 Detlef Müller<sup>4</sup>

6 <sup>1</sup>Purdue University, West Lafayette, IN, United States

7 <sup>2</sup>NASA Langley Research Center, Hampton, VA, United States

8 <sup>3</sup>Science Systems and Applications, Inc./NASA Langley Research Center, Hampton, VA, United States

9 <sup>4</sup>University of Hertfordshire, Hatfield, Hertfordshire, United Kingdom

10 *Correspondence to:* H. Harshvardhan (harshvar@purdue.edu)

11 **Abstract.** Biomass burning in southwestern Africa produces smoke plumes that are transported over the Atlantic  
12 Ocean and overlie vast regions of stratocumulus clouds. This aerosol layer contributes to direct and indirect radiative  
13 forcing of the atmosphere in this region, particularly during the months of August, September and October. There was  
14 a multi-year international campaign to study this aerosol and its interactions with clouds. Here we report on the  
15 evolution of aerosol distributions and properties as measured by the airborne high spectral resolution lidar (HSRL-2)  
16 during the ORACLES (Observations of Aerosols above Clouds and their intEractionS) campaign in September 2016.  
17 The NASA Langley HSRL-2 instrument was flown on the NASA ER-2 aircraft for several days in September 2016.  
18 Data were aggregated at two pairs of 2°×2° grid boxes to examine the evolution of the vertical profile of aerosol  
19 properties during transport over the ocean. Results showed that the structure of the profile of aerosol extinction and  
20 microphysical properties is maintained over a one to two-day time scale. In the 3-5 km altitude range, 95% of the  
21 aerosol extinction was contributed by particles in the 0.05-0.50 μm radius size range, with the aerosol in this size  
22 range having an average effective radius of 0.16 μm. This indicates that there is essentially no scavenging or dry  
23 deposition at these altitudes. Moreover, there is very little day to day variation in these properties, such that time  
24 sampling as happens in such campaigns, may be representative of longer periods such as monthly means. Below 3 km  
25 there is considerable mixing with larger aerosol, most likely continental source near land. Furthermore, these  
26 measurements indicated that there was often a distinct gap between the bottom of the aerosol layer and cloud tops at  
27 the selected locations as evidenced by a layer of several hundred meters that contained relatively low aerosol extinction  
28 values above the clouds.

## 29 1 Introduction

30 Aerosols are often considered as the most confounding element in the climate system when simulating parameters of  
31 the Earth's current climate. Their interaction with clouds makes the problem extremely complicated. The general topic  
32 of aerosol-cloud interaction has been of great interest in the scientific community: to quote the report of the  
33 Intergovernmental Panel on Climate Change (IPCC AR5) "Clouds and aerosols continue to contribute the largest  
34 uncertainty to estimates and interpretations of the Earth's changing energy budget" (Boucher et al., 2013).

35 In the context of these interactions, the interplay of biomass burning (BB) aerosol and the stratocumulus clouds in  
36 the Southeast (SE) Atlantic is unique and crucial to the estimates of the energy budget of the region. This BB aerosol  
37 arises from the seasonal burning (July-October) of agricultural residue in the southwestern African Savannah and  
38 traverses large distances westward over the SE Atlantic Ocean. Unlike the aerosol from industrial activity and biofuels  
39 that intermingle with clouds in many regions (Ramanathan et al., 2001; Mechoso et al., 2013), these optically thick  
40 BB aerosol layers overlay vast stretches of marine stratus cloud in the SE Atlantic (Chand et al., 2009; Wilcox, 2010;  
41 Adebisi et al., 2015) where they have a direct radiative effect. The BB aerosol can also act as nuclei for cloud droplets  
42 and so cause a potentially significant cloud albedo effect. Observations and modelling studies of such interactions in  
43 the Southeast Atlantic and southern Africa regions include Diamond et al. (2018), Kacarab et al. (2020), Mallet et al.  
44 (2020) and Gupta et al. (2022). There is also some evidence that aerosol can alter the thermodynamics of cloud  
45 formation through semi-direct effects (Sakaeda et al., 2011). Studies using high resolution limited area models have  
46 shown a variety of effects, including stratus to cumulus transition resulting from these interactions (Yamaguchi et al.,  
47 2015; Gordon et al., 2018; Lu et al., 2018). The semi-direct effect has also been shown to be important in a limited  
48 time run of a global model (Das et al., 2020).

49 During the course of its transport over the Atlantic basin, the dense BB aerosol layer affects the underlying clouds  
50 and Earth's radiative balance in multiple ways. It exerts a direct radiative forcing (DRF) by scattering and absorbing  
51 solar radiation in the atmosphere; when clouds are present, these aerosols absorb incoming solar radiation along with  
52 the radiation reflected by the underlying cloud surface (Chand et al., 2009; Meyer et al., 2013; Zhang et al., 2016).  
53 Simultaneously, depending on the relative vertical location of the aerosol with respect to the cloud deck, the cloud  
54 cover (fraction) or liquid water path may increase or decrease in response to heating of surrounding air masses due to  
55 aerosol absorption and subsequent changes in atmospheric stability, the semi-direct forcing (Sakaeda et al., 2011;  
56 Wilcox, 2012; Das et al., 2020). Observations at Ascension Island show that daytime cloud cover and relative humidity  
57 are lower when there is more smoke in the marine boundary layer (Zhang and Zuidema, 2019). Moreover, as the  
58 marine boundary layer (MBL) deepens farther offshore and north of 5° S, subsiding aerosol particles become entrained  
59 into the MBL and interact with the clouds as cloud condensation nuclei to affect their microphysics (indirect forcing)  
60 (Costantino and Breon, 2013; Painemal et al., 2014).

61 In the context of simulating the above alluded aerosol radiative effects, it is vital that aerosol-cloud overlap  
62 characteristics are accurately represented within the models. The quantification of these aerosol-cloud overlap  
63 characteristics in the models is necessary for a variety of reasons. For example, previous studies have found that the  
64 sign and magnitude of DRF of absorbing aerosol above clouds (AAC) critically depends upon the reflectance and  
65 coverage of the underlying cloud surfaces along with the optical properties, composition and size distribution of the  
66 overlying aerosols (Keil and Haywood, 2003; Chand et al., 2009). Additionally, the magnitude and sign of the aerosol  
67 semi-direct effects are quite sensitive to the vertical distribution of aerosols, especially with respect to the vertical  
68 location of clouds (Penner et al., 2003; McFarquhar and Wang, 2006; Koch and Del Genio, 2010).

69 Here we address the evolution of the vertical properties of BB aerosol as it travels in the marine environment after  
70 leaving the African land mass. Section 2 identifies the field campaign and specifies the geographic region selected for  
71 the analysis and rationale for that choice. Section 3 describes the attributes of the instrument and key parameters

Deleted: 1

73 related to the aerosol that can be extracted from the measurements. Section 4 presents the results followed by a  
74 summary and conclusion in section 5.

## 75 **2 Field Campaigns**

76 The concerns mentioned above were the driving force behind plans for several international multi-year field  
77 campaigns; ORACLES (Observations of Aerosols above Clouds and their intEractionS, Redemann et al., 2021),  
78 CLARIFY-2017 (CLoud-Aerosol-Radiation Interactions and Forcing for Year 2017, Haywood et al., 2021), and  
79 LASIC (Layered Atlantic Smoke Interactions with Clouds, Zuidema et al., 2016, 2018). A key component of the  
80 September 2016 NASA ORACLES Intensive Observation Period (IOP) was the vertical profiling of aerosol properties  
81 measured by an airborne lidar, the NASA Langley High Spectral Resolution Lidar-2, HSRL-2 (Burton et al., 2018),  
82 on-board the NASA ER-2, which was based in Walvis Bay, Namibia, for operations during 2016, the deployment  
83 covered in this study. In the following two years, the instrument was on-board the P-3 flying out of São Tomé. The  
84 siting and flight tracks chosen ensured adequate coverage of the seasonal BB aerosol.

### 85 **2.1 Meteorology**

86 The September monthly mean meteorological situation is shown in Fig. 1 from MERRA2 reanalysis (Buchard et  
87 al., 2017; Randles et al., 2017) along with locations of relevant sites. A thorough meteorological analysis for all  
88 ORACLES deployments is provided in Ryoo et al. (2021). For the period under consideration here, they found that  
89 the African Easterly Jet-South (AEJ-S), fast moving zonal easterlies centered on 650 hPa around 5-15°S, was active  
90 and corresponded closely to the long-term climatology. Fig. 2 shows 650 hPa winds from MERRA2 reanalysis at the  
91 beginning, at the end, and on two intermediate days during which HSRL-2 measurements were made. ER-2 flight  
92 tracks during the September 2016 IOP are shown in Fig. 3. Note that flights were primarily confined to within roughly  
93 1000 km of the African coast with only the 22 September flight venturing further. Flights such as executed during the  
94 IOP are unable to follow air parcels in a Lagrangian fashion to examine the evolution of smoke plumes. Here we  
95 provide an alternate framework by which to study evolving aerosol properties in an average sense. In order to establish  
96 average characteristics of the BB smoke plume as it travels over the ocean, we have chosen five grid boxes of two-  
97 degree latitude and longitude on a side at various distances from the source and aggregated observations. The choice  
98 of grid boxes was based on the availability of data from the flights (Fig. 3) and the general direction of transport of  
99 the smoke as evidenced by the wind fields in Fig. 2. The grid boxes so chosen are marked on Figs. 2 and 3 and the  
100 rationale for the choice is explained below.

101 Figure 4 shows 48-hour backward trajectory frequency analyses at 3.5 km, roughly the central altitude of the plume,  
102 using NOAA HYSPLIT trajectory calculations ([https://www.ready.noaa.gov/HYSPLIT\\_traj.php](https://www.ready.noaa.gov/HYSPLIT_traj.php)) which were carried  
103 out using archived GDAS 0.5-degree meteorology (Stein et al., 2015). The frequency distribution is a 48-hour history  
104 of the paths taken by air parcels arriving at the grid boxes marked A and C at 3500 m altitude. The time period of the  
105 frequency analyses covers the entire period during which HSRL-2 measurements were made, 12-24 September 2016.

106 The selected grid box pairs indicate that Box A receives aerosol that has earlier crossed Box B and Box C is downwind  
107 of Box D; boxes B and D receive aerosol directly from BB sources on land. The grid box pairs A/B and C/D can  
108 therefore provide information on the evolution of the microphysics and vertical distribution of BB aerosol plumes  
109 after leaving the continent. This strategy is similar to that used in comparisons of models with observations for this  
110 campaign by Shinozuka et al. (2020), who also showed that observations made on the sampled days were  
111 representative of monthly means. In addition to the four boxes strongly influenced by smoke, a southern box, E, has  
112 been chosen to provide a control contrast to the other areas in that it is influenced primarily by maritime air as seen  
113 from Figs. 1 and 2.

## 114 2.2 ORACLES 2016 IOP

115 The days during the campaign that were included in the averaging procedure are shown in Table 1. Also included  
116 is the typical time of the day when the measurements were made, a function of the flight pattern of the ER-2. The  
117 number of lidar return profiles averaged for each grid box and statistics related to the backward trajectories are also  
118 listed. These grid boxes contained aircraft tracks on multiple days during which trajectory analysis showed near-  
119 uniform wind direction between 2.5 and 4.5 km altitude throughout the IOP. With the exception of the grid box  
120 centered at 22° S, 9° E, all indicate flow from the source region of BB aerosol. Table 1 also lists the mean and standard  
121 deviation of time duration in hours spent over water of air parcels arriving at 3500 m altitude at the grid box during  
122 the averaging period. There is no entry for Box E since arriving air had a maritime source and did not originate from  
123 land. It must be stressed that the duration is not calculated from the source region on land, which is distributed over a  
124 large area of central Africa (e.g., Fig. 9 of Redemann et al., 2021) and cannot be uniquely identified with specific  
125 observations made over the ocean. The plume has already been airborne over land for several hours (see Fig. 4) and  
126 aerosol would have undergone transformations that occur at short time scales (Cappa et al., 2020). The duration was  
127 calculated by running HYSPLIT backward trajectories of air parcels arriving every six hours starting at 0600 UTC on  
128 the days of the first flight and ending at 1800 UTC on the days of the last flight of the averaging period and is shown  
129 in some detail in Fig. 5, which essentially reflects the profile of the prevailing wind speeds. The inference is that BB  
130 smoke at 3500 m altitude arrives at A on average about 30 h after passing B and arrives at C 35 h after passing D. The  
131 change in selected aerosol properties as measured by the HSRL-2 during this travel in the marine environment provides  
132 information on the evolution of the plume during this time period.

## 133 3 HSRL-2

134 The NASA LaRC HSRL-2 uses the HSRL technique to independently retrieve aerosol extinction and backscatter  
135 (Shipley et al., 1983; Grund and Eloranta, 1991; She et al., 1992) without a priori assumptions on aerosol type or  
136 extinction-to-backscatter ratio. By using the HSRL technique, HSRL-2, like its predecessor HSRL-1 (Hair et al.,  
137 2008), provides accurate backscatter profiles even in situations where the lidar beam is attenuated by overlying cloud  
138 or aerosol as long as it is not completely attenuated. The LaRC HSRL-2 employs the HSRL technique at 355 and 532

139 nm and the standard backscatter technique at 1064 nm. It also measures aerosol and cloud depolarization at all three  
140 wavelengths. The HSRL-2 provides vertically resolved measurements of the following extensive and intensive aerosol  
141 parameters below the aircraft (approximate archival horizontal,  $\Delta x$ , and vertical resolutions,  $\Delta z$ , are listed assuming  
142 ER-2 cruise speed).

143 • *Extensive parameters*<sup>1</sup> – backscatter coefficient,  $\beta$ , at 355, 532 and 1064 nm ( $\Delta x \sim 2$  km,  $\Delta z \sim 15$  m); extinction  
144 coefficient,  $\alpha$ , at 355, and 532 nm ( $\Delta x \sim 12$  km,  $\Delta z \sim 300$  m); optical depth at 355 and 532 nm (integrating the profile  
145 of extinction). The aerosol optical depth (AOD) is a critical quantity in discussions of the influence of aerosol on  
146 climate (Boucher et al., 2013).

147 • *Intensive parameters* – extinction-to-backscatter ratio of aerosol, the Lidar Ratio,  $S_a = \alpha_a / \beta_a$ , at 355 and 532 nm  
148 ( $\Delta x \sim 12$  km,  $\Delta z \sim 300$  m); depolarization,  $\delta_a = \beta_a^\perp / \beta_a^\parallel$ , at 355, 532, and 1064 nm ( $\Delta x \sim 2$  km,  $\Delta z \sim 15$  m); and  
149 aerosol backscatter wavelength dependence (i.e., Ångström exponent for aerosol backscatter – directly related to the  
150 backscatter color ratio) for two wavelength pairs (355-532 and 532-1064 nm,  $\Delta x \sim 2$  km,  $\Delta z \sim 15$  m).

151 The overall systematic error associated with the backscatter calibration is estimated to be less than 5 % for the 355  
152 and 532 nm channels and 20 % for 1064 nm (Burton et al., 2015). Under typical conditions, the total systematic error  
153 for extinction is estimated to be less than 0.01 km<sup>-1</sup> at 532 nm. The random errors for all aerosol products are typically  
154 less than 10 % for the backscatter and depolarization ratios (Hair et al., 2008). Rogers et al. (2009) validated the HSRL  
155 extinction coefficient profiles and found that the HSRL extinction profiles are within the typical state-of-the-art  
156 systematic error at visible wavelengths (Schmid et al., 2006). Since HSRL-2 includes the capability to measure  
157 backscatter at three wavelengths and extinction at two wavelengths, “3 $\beta$ +2 $\alpha$ ” microphysical retrieval algorithms  
158 (Müller et al., 1999a, 1999b; Veselovskii et al., 2002) are used to retrieve height-resolved parameters such as aerosol  
159 effective radius and number, surface and volume concentrations (Müller et al., 2014, Sawamura et al., 2016). Here we  
160 restrict ourselves to the effective radius of the particles.

## 161 4 Results

162 In this study of the vertically resolved evolving properties of BB aerosol, we present key lidar measurements and  
163 microphysical results obtained by performing the “3 $\beta$ +2 $\alpha$ ” retrieval mentioned in Section 3.

164  
165

---

<sup>1</sup> By the term *extensive*, we refer to optical parameters, such as extinction, that are influenced by the amount (concentration) and type (size, composition, shape) of aerosol/cloud particles. *Intensive* properties, on the other hand, are those that depend only on the nature of the particles and not on their quantity or concentration, but rather depend only on aerosol type (Anderson et al., 2003).

166 **4.1 Lidar**

167 Vertical profiles averaged over the times of overflight in  $2^\circ \times 2^\circ$  latitude/longitude boxes shown in Figure 3 on the  
168 days given in Table 1 are for the following properties.

- 169 1. Aerosol Extinction at 532 nm,  $\alpha_a$ , determined by aerosol number concentration, microphysical  
170 properties and relative humidity
- 171 2. Backscatter Ångström exponent between 1064 and 532 nm, an indication of particle size.
- 172 3. Aerosol Depolarization at 532 nm, a measure of particle asphericity.
- 173 4. Aerosol extinction to backscatter ratio, the Lidar Ratio, at 532 nm, a marker for aerosol composition.

174 Inspection of the wind field at 650 hPa in Fig. 2 and backward trajectory frequency plots in Fig. 4 suggest that the  
175 grid boxes chosen fit naturally into two pairs of tracks of the widespread BB aerosol field. The northern pair, identified  
176 in Table 1 as A and B, centered around  $10^\circ$  S, are in a faster zonal track, whereas the grid boxes C and D are in a track  
177 centered between  $13$ - $15^\circ$  S that is slightly slower and has a component from the north over a stretch of water (Fig. 2).  
178 The two pairs can then provide information on the evolution of aerosol properties over a time scale of one to two days.  
179 Figures 6-9 show the aerosol extinction, backscatter Ångström exponent, aerosol depolarization and Lidar Ratio for  
180 the two pairs of grid boxes and Box E, which is at the southern edge of the region influenced by the BB aerosol. The  
181 results presented are one-minute averages of independent 10 s vertical profiles for backscatter Ångström exponent  
182 and depolarization and one-minute averages for extinction and lidar ratio profiles. From Table 1, the mean time elapsed  
183 between B and A is 29.4 h and that between D and C is 34.9 h. It should be pointed out that parameter values shown  
184 below the level of mean cloud top are averages of lidar returns through breaks in the stratus deck and are not relevant  
185 for this study. If we use the low cut-off of an extinction coefficient of  $15 \text{ Mm}^{-1}$  to indicate an aerosol-free layer  
186 (Shinozuka et al., 2020), then Fig. 6 indicates that the bulk of the smoke layers encountered at these distances from  
187 land were separated from the cloud top, a feature more prevalent during the 2016 IOP than in 2017 and 2018  
188 (Redemann et al., 2021).

189 The northern plume is a column of aerosol of relatively constant extinction from just above 2.5 km to 5 km while  
190 the southern plume has a profile of extinction that increases nearly linearly with height from a minimum near the cloud  
191 top to a maximum at 5 km (Fig. 6). The vertical structure of the aerosol profiles measured by HSRL-2 was compared  
192 to water vapor profiles represented by the Modern-Era Retrospective analysis for Research and Applications, Version  
193 2 (MERRA2) model. Pistone et al. (2021) explored the relationship between aerosols, CO, water vapor as measured  
194 by ORACLES airborne in situ measurements and represented by models including MERRA2. They found the  
195 MERRA2 water vapor profiles, like the measured water vapor profiles, exhibited a linear relationship with CO and  
196 biomass burning plume strength; they also found that smoky, humid air produced by daytime convection over the  
197 continent advected over the ocean and into the ORACLES study region. MERRA2 water vapor profiles produced at  
198 three hourly increments and 72 pressure levels were interpolated to the times and locations of the HSRL-2 profiles.  
199 Water vapor mixing ratio generally decreased significantly just above the PBL then increased for altitudes around 2  
200 to 3 km before decreasing again. This behavior is generally consistent with the relationship between water vapor and  
201 aerosol scattering reported by Pistone et al. (2021).

202 Figure 10 shows the median, 25<sup>th</sup> and 75<sup>th</sup> percentile relative humidity (RH) profiles computed by interpolating the  
203 MERRA2 0.5-deg. 3-hourly humidity profiles to the locations and times of the HSRL-2 measurements. The profiles  
204 typically show a more pronounced increase in RH with altitude that more closely follows the HSRL-2 measurements  
205 of aerosol extinction profiles, although the MERRA2 profiles typically begin decreasing above 4 km whereas the  
206 airborne in situ RH measurements and HSRL-2 aerosol extinction profiles begin decreasing above 5 km. Interestingly,  
207 during three of the dates (Sept. 12, 16, 22) considerable portions of the smoke layers correspond to MERRA2 relative  
208 humidity above 60-70%. This increase in RH with altitude could help explain at least some of the increase in aerosol  
209 extinction with height observed in the HSRL-2 profiles of the C/D Box pair. Aerosol humidification often amplified  
210 the increase in aerosol extinction by factors of 1.5 or more (Doherty et al., 2022).

211 The Ångström exponent (Fig. 7) and depolarization (Fig. 8) indicate the presence of fine spherical particles at the  
212 top of the plume and increasing sizes towards the bottom. The Lidar Ratio (Fig. 9) above 3 km for the two pairs is  
213 between 70 and 80 sr, suggesting strong absorption (Müller et al., 2019) but is considerably less and highly variable  
214 in Box E and in the lower layers of the aerosol plume in Box D, where the smoke plume most likely has components  
215 of continental aerosol such as dust and pollution typical of the nearby Namibian coast (Klopper et al., 2020). The most  
216 striking feature of the results is the very small profile-to-profile variability of the intensive lidar parameters in the  
217 upper two kilometers of the plume over the course of several days as evident from the range of values in the 25-75  
218 percentile shaded grey in Figs. 7-9. This suggests strongly that the particles maintain their size, shape and absorbing  
219 properties over the first few days of transport over the ocean. This result is of some importance for climate studies in  
220 which the radiative properties of BB aerosol are input to the calculation of radiative forcing. Complex chain aggregates  
221 as found near the source of fires (Pósfai et al., 2003, China et al., 2013) are typically not represented in climate models.  
222 However, if the aerosol is already spherical and maintains its size over the time period of radiative interactions being  
223 studied, then core-shell models of varying degrees of complexity could perhaps suffice (Zhang et al., 2020). The lower  
224 portion of the plume containing larger BB aerosol particles is subject to mixing with marine and continental particles  
225 from regions not affected by biomass burning and is highly variable in nature. This would be more difficult to model  
226 but Fig. 6 shows that the aerosol extinction coefficient decreases rapidly at lower levels so errors in representation  
227 may be acceptable.

## 228 4.2 Microphysics

229 The lidar measurements are inverted to obtain information regarding particle size. The inversion is performed on one-  
230 minute averages of six independent 10 s backscatter profiles and one-minute average extinction profiles. Details of  
231 the inversion process are in Müller et al. (2019) and references therein. The particle size distribution is represented  
232 using a series of eight triangular basis functions that can represent both monomodal and bimodal size distributions  
233 (*ibid*). Points to note are that the procedure makes the following assumptions: the particles are spherical and  
234 homogeneous having wavelength-independent complex index of refraction. The low (< 5 %) values of depolarization  
235 through most of the plume, shown in Fig. 8, suggests that the spherical assumption is justified. There is most likely  
236 structure and inhomogeneity in the core of the particles, but current particle optical models are unable to incorporate

237 these complexities. Results from this inversion procedure have been compared to coincident airborne in situ particle  
238 measurements. Müller et al. (2014) present results from a campaign off the northeast coast of the US showing that the  
239 inversion results agree with in situ measurements of effective radius and also number, surface area and volume  
240 concentration within error bars. Sawamura et al. (2017) report on campaigns in the wintertime San Joaquin Valley of  
241 California and summertime near Houston, TX. They found high correlation and low bias in surface and volume  
242 concentration in situ measurements relative to HSRL with the best agreement for submicron fine-mode aerosol, which  
243 is most relevant to the current study. Müller et al. (2019) report retrievals and their uncertainty for one day in the  
244 ORACLES campaign, 22 September 2016. Considering only optical data with strong signal-to-noise ratio, they  
245 estimate retrieval errors are 25 % for number concentration. The relative uncertainty in effective radius for parts of  
246 the flight track where particle size was nearly constant was below 20 %.

247 In order to help separate particles that have BB source from coarser particles of continental or marine origin, we  
248 specify a Submicron Fraction (SMF) as the contribution to the extinction at 532 nm of particles in the radius range  
249 0.05-0.50  $\mu\text{m}$  (Anderson et al., 2005). Figure 11 shows the profiles of SMF for the five grid boxes and not surprisingly,  
250 the bulk of the smoke plume, especially between 3 and 5 km contains aerosol almost entirely in the submicron range.  
251 Below 3 km, at locations both near and further way from the coast, there is a marked increase in the fraction of larger  
252 particles. The increase in depolarization (Fig. 8) at these lower levels and a decrease in the Lidar Ratio (Fig. 9) suggest  
253 mixing with the aforementioned non-BB aerosol particles. However, the sharp decrease in extinction below 3 km (Fig.  
254 6) indicates that their contribution to direct radiative effects would be minimal. Finally, Fig. 12 shows the vertical  
255 profile of the effective radius of the SMF aerosol population. The effective radius is 0.16  $\mu\text{m}$  with little variation  
256 between 3 and 5 km. Of greater significance is that it remains very similar between the pairs of grid boxes along the  
257 transport trajectory of the smoke. The retrieved effective radius is similar to the results presented by Müller et al.  
258 (2014) for a mixture of urban aerosol and smoke. Their comparison with in situ measurements showed a slight  
259 overestimate but within a standard deviation. The retrieved and in situ results also show that the particle size is uniform  
260 with altitude even when the number concentration drops by a factor of three. Another set of prior comparisons of  
261 HSRL-2 and in situ measurements is provided in Sawamura et al. (2017). Here again, the effective radius of the  
262 submicron fraction of particles, 0.15  $\mu\text{m}$ , is uniform with altitude, and comparable though biased slightly low  
263 compared to in situ observations.

264 The effective radii of the SMF aerosols, which typically vary between 0.15 to 0.20  $\mu\text{m}$ , are generally consistent  
265 with the sizes reported previously for smoke aerosol in the ORACLES region. Haywood et al. (2021) provide a  
266 composite of the aerosol sizes for biomass burning aerosol off the South African coast. These size distributions, which  
267 were derived from airborne in situ measurements (Haywood et al., 2003; Peers et al., 2019; Wu et al., 2020), typically  
268 correspond to SMF aerosol effective radii between 0.14-0.17  $\mu\text{m}$  and were for the dry aerosol. [Shinozuka et al. \(2020\)](#)  
269 [reported on airborne aerosol sizes measured during ORACLES by an Ultra-High-Sensitivity-Aerosol Spectrometer](#)  
270 [\(UHSAS\) deployed on the NASA P-3 aircraft. The UHSAS measured particles with dry diameters between 60 and](#)  
271 [1000 nm. SMF aerosol effective radii derived from the UHSAS measurements of volume mean diameter were](#)  
272 [generally around 0.09-0.10  \$\mu\text{m}\$  for the dry aerosol. Shinozuka et al. \(2020\) noted that the UHSAS measurements were](#)  
273 [somewhat undersized and so were adjusted to account for this effect; this adjustment improved scattering closure with](#)



274 coincident nephelometer measurements. As discussed in section 4.1, the RH on some days was above 60-70% so that  
275 effective radii under ambient conditions could be expected to be somewhat higher than for the dry aerosol. Using  
276 measurements from an airborne Differential Aerosol Sizing and Hygroscopicity Spectrometer Probe (DASH-SP),  
277 Shingler et al. (2016) quantified the size-resolved growth factors for several aerosol types; they found that at RH~70-  
278 80%, particle diameters for biomass burning aerosols were about 15-20% larger than for the dry aerosol. Xu et al.  
279 (2021) derived aerosol properties during the 2016 ORACLES mission using an inversion algorithm that combined  
280 HSRL-2 and Research Scanning Polarimeter (RSP) remote sensing measurements. These retrieved aerosol properties  
281 were then compared with those derived from the UHSAS measurements described by Shinozuka et al. (2020). For  
282 measurements acquired on Sept. 12, 2016, the SMF aerosol effective radius derived from the remote sensing  
283 measurements were generally between 0.12-0.15  $\mu\text{m}$  and were only slightly (0.012  $\mu\text{m}$ ) higher than the effective radii  
284 for the (dry) SMF aerosol derived from the UHSAS measurements. This suggests that some of this difference is  
285 associated with differences in RH between the remote sensing retrievals and the in situ measurements.

Deleted: airborne in situ

Deleted: airborne in situ size distribution

## 286 5 Conclusions

287 The results of the aggregated HSRL-2 profiles during the 2016 ORACLES IOP presented here show two main  
288 findings. These are however limited to a brief period in the transport of BB smoke from continental Africa over marine  
289 clouds in the Atlantic Ocean. This is a limitation of the 2016 campaign because the flight tracks remained within 1000  
290 km of the coast. For the period of one to two days after crossing the land-ocean boundary, the fraction of all particles  
291 that are in the submicron range in the main smoke plume between 3 and 5 km is around 95 %. The effective radius of  
292 the submicron particles in this altitude interval is 0.16  $\mu\text{m}$  and essentially constant with altitude. The particle size is  
293 comparable to measured particle sizes in previous campaigns that sampled aerosol that was a mixture of urban haze  
294 and smoke (Müller et al., 2014; Sawamura et al., 2017). Moreover, the shape of the median vertical profile of  
295 extinction does not change during the first two days of transport over water suggesting the absence of dry deposition  
296 and wet scavenging. The low ( $< 0.05$ ) depolarization ratio of the submicron particles signifies that they are well coated  
297 and the assumption of sphericity in the inversion procedure and models that estimate the radiative effects of aerosol  
298 is justified. The BB aerosol mix with continental and marine aerosol at the base of the plume but during the September  
299 2016 IOP this layer of mixed aerosol tended to have very low extinction coefficients suggesting low abundance and  
300 there was often a distinct gap between the plume and the cloud tops.

301 The HSRL-2 instrument was also deployed in the 2017 and 2018 ORACLES campaigns but was deployed on the  
302 NASA P-3 which often flew at low altitude to acquire in situ measurements of aerosols and clouds. Consequently, the  
303 HSRL-2 was not able to make continuous measurements of the BB aerosol plumes in a manner similar as when  
304 deployed on the ER-2. However, there are segments of the track that can provide similar information to the data  
305 obtained in the 2016 campaign but for a different time period. Moreover, some flight tracks extended much further  
306 from land (Doherty et al., 2021). Analysis of the later campaigns will provide information on the physical evolution  
307 of aerosol that has aged for a longer period than is covered in this study.

310 **Data Management**

311 HSRL-2 optical data and retrieved inversion data are available at the NASA archive site  
312 <https://espoarchive.nasa.gov/archive/browse/oracles/id8/ER2> and are permanently archived at  
313 doi:10.5067/SUBORBITAL/ORACLES/ER2/2016\_V1.

314 **Acknowledgements**

315 The lead author would like to thank NASA Langley Research Center for hosting him during a sabbatical when this  
316 study was initiated. HSRL-2 participation in ORACLES was supported by NASA through the Earth Venture  
317 Suborbital-2 (EVS-2) program (grant no. 13-EVS2-13-0028). Funding for this work was also provided by NASA  
318 through the Radiation Sciences Program. We wish to thank the NASA ER-2 pilots and ground crew for their extensive  
319 support during ORACLES.

320

321 **References**

322 Anderson, T. L., Charlson, R. J., Winker, D. M., Ogren, J. A., and Holmén, K.: Mesoscale variations of tropospheric  
 323 aerosols, *J. Atmos. Sci.*, 60(1), 119-136, 2003.

324 Anderson, T. L., Wu, Y., Chu, D. A., Schmid, B., Redemann, J., and Dubovik, O.: Testing the MODIS satellite  
 325 retrieval of aerosol fine-mode fraction, *J. Geophys. Res.*, 110, D18204, doi:10.1029/2005JD005978, 2005.

326 Adebiyi, A. A., Zuidema, P., Chang, I., Burton, S. P., and Cairns, B.: Mid-level clouds are frequent above the Southeast  
 327 Atlantic stratocumulus clouds, *Atmos. Chem. Phys.*, 20, 11025-11043, doi:10.5194/acp-20-11025-2020, 2020.

328 Boucher, O., Randall, D., Artaxo, P., Bretherton, C., Feingold, G., Forster, P., Kerminen, V.-M. Kondo, Y., Liao, H.,  
 329 Lohmann, U., Rasch, P., Satheesh, S. K., Sherwood, S., Stevens, B., and Zhang X.Y.: Clouds and Aerosols. In:  
 330 Climate Change 2013: The Physical Science Basis. Contribution of Working Group I to the Fifth Assessment Report  
 331 of the Intergovernmental Panel on Climate Change [Stocker, T. F., Qin, D., Plattner, G.-K., Tignor, M., Allen, S.  
 332 K., Boschung, J., Nauels, A., Xia, Y., Bex V., and Midgley, P. M. (eds.)]. Cambridge University Press, 2013.

333 Buchard, V., Randles, C. A., da Silva, A. M., Darnenov, A., Colarco, P. R., Govindaraju, R., Ferrare, R. A., Hair, J.,  
 334 Beyersdorf, A. J. Ziemba L. D., and Yu, H.: The MERRA-2 aerosol reanalysis, 1980 onwards Part II: Evaluation  
 335 and case studies, *J. Climate*, 30, 6851-6871, doi:10.1175/JCLI-D-16-0613.1, 2017.

336 Burton, S. P., Hostetler, C. A., Cook, A. L., Hair, J. W., Seaman, S., Scola, S., Harper, D. B., Smith, J. A., Fenn, M  
 337 A., Ferrare, R. A., Saide, P. E., Chemyakin, E. V., and Müller, D.: Calibration of a high spectral resolution lidar  
 338 using a Michelson interferometer with data examples from ORACLES, *Appl. Optics*, 57, 6061-6075, 2018.

339 Burton, S. P., Hair, J. W., Kahnert, M., Ferrare, R. A., Hostetler, C. A., Cook, A. L., Harper, D. B., Berkoff, T. A.,  
 340 Seaman, S. T., Collins, J. E., Fenn, M. A., and Rogers, R. R.: Observations of the spectral dependence of linear  
 341 particle depolarization ratio of aerosols using NASA Langley airborne High Spectral Resolution Lidar, *Atmos.*  
 342 *Chem. Phys.*, 15, 13453–13473, doi.org/10.5194/acp-15-13453-2015, 2015.

343 Cappa, C. D., Lim, C. Y., Hagan, D. H., Coggon, M., Koss, A., Sekimoto, K., de Gouw, J., Onasch, T. B., Warneke,  
 344 C., and Kroll, J. H.: Biomass-burning-derived particles from a wide variety of fuels – Part 2: Effects of  
 345 photochemical aging on particle optical and chemical properties, *Atmos. Chem. Phys.*, 20, 8511-8532,  
 346 doi:10.5194/acp-20-8511-2020, 2020.

347 Chand, D., Wood, R., Anderson, T. L., Satheesh, S. K., and Charlson, R. J.: Satellite-derived direct radiative effect of  
 348 aerosols dependent on cloud cover, *Nat. Geosci.*, 2, 181-184, doi:10.1038/Ngeo437, 2009.

349 China, S., Mazzoleni, C., Gorkowski, K., Aiken, A. C., and Dubey, M. K.: Morphology and mixing state of individual  
 350 freshly emitted wildfire carbonaceous particles, *Nat. Commun.*, 4:2122 doi: 10.1038/ncomms3122, 2013.

351 Costantino, L., and Bréon F. M.: Aerosol indirect effect on warm clouds over South-East Atlantic from co-located  
 352 MODIS and CALIPSO observations, *Atmos. Chem. Phys.*, 13, 69-88, doi:10.5194/acp-13-69-2013, 2013.

353 Das, S., Harshvardhan, H., and Colarco, P. R.: The influence of elevated smoke layers on stratocumulus clouds over  
 354 the SE Atlantic in the NASA Goddard Earth Observing System (GEOS) Model, *J. Geophys. Res. Atmos.*, 125,  
 355 e2019JD031209. doi:10.1029/2019JD031209, 2020.

356 Diamond, M. S., Dobracki, A., Freitag, S., Small Griswold, J. D., Heikkilä, A., Howell, S. G., Kacarab, M. E.,  
 357 Podolske, J. R., Saide, P. E., and Wood, R.: Time-dependent entrainment of smoke presents an observational  
 358 challenge for assessing aerosol–cloud interactions over the southeast Atlantic Ocean, *Atmos. Chem. Phys.*, 18,  
 359 14623–14636, https://doi.org/10.5194/acp-18-14623-2018, 2018.

360 Doherty, S. J., Saide, P. E., Zuidema, P., Shinozuka, Y., Ferrada, G. A., Gordon, H., Mallet, M., Meyer, K.,  
 361 Painemal, D., Howell, S. G., Freitag, S., Dobracki, A., Podolske, J. R., Burton, S. P., Ferrare, R. A., Howes, C.,  
 362 Nabat, P., Carmichael, G. R., da Silva, A., Pistone, K., Chang, I., Gao, L., Wood, R., and Redemann, J.: Modeled  
 363 and observed properties related to the direct aerosol radiative effect of biomass burning aerosol over the Southeast  
 364 Atlantic, *Atmos. Chem. Phys.*, 22, 1-46, https://doi.org/10.5194/acp-22-1-2022, 2022.

365 Gordon, H., Field, P. R., Abe, S. J., Dalvi, M., Grosvenor, D. P., Hill, A. A., Johnson, B. T., Miltenberger, A. K.,  
 366 Yoshioka, M., and Carslaw, K. S.: Large simulated radiative effects of smoke in the south-east Atlantic, *Atmos.*  
 367 *Chem. Phys.*, 18, 15261-15289, doi:10.5194/acp-18-15261-2018, 2018.

368 Grund, C. J., and Eloranta, E. W.: University of Wisconsin high spectral resolution lidar, *Opt. Eng.*, 30, 6-12, 1991.

369 Gupta, S., McFarquhar, G. M., O'Brien, J. R., Poellot, M. R., Delene, D. J., Miller, R. M., and Small Griswold, J. D.:  
 370 ~~Factors affecting precipitation formation and precipitation susceptibility of marine stratocumulus with variable~~  
 371 ~~above- and below-cloud aerosol concentrations over the Southeast Atlantic, *Atmos. Chem. Phys.*, 22, 2769-2793,  
 372 ~~<https://doi.org/10.5194/acp-22-2769-2022>, 2022.~~~~

373 Hair, J. W., Hostetler, C. A., Cook, A. L., Harper, D. B., Ferrare, R. A., Mack, T. L., Welch, W., Izquierdo, L. R.,  
 374 Hovis, F. E.: Airborne High Spectral Resolution Lidar for profiling aerosol optical properties, *Appl. Optics*, 47, doi:  
 375 10.1364/AO.47.006734, 2008.

- Deleted: P
- Deleted: S
- Deleted: M
- Deleted: S
- Deleted: V
- Deleted: A
- Deleted: B
- Deleted: C
- Deleted: A
- Deleted: C
- Deleted: Discuss. [preprint]
- Deleted: [2021-677, in review, 2021](#)

388 Haywood, J. M., Osborne, S. R., Francis, P. N., Keil, A., Formenti, P., Andreae, M. O., and Kaye, P. H.: The mean  
389 physical and optical properties of regional haze dominated by biomass burning aerosol measured from the C-130  
390 aircraft during SAFARI 2000, *J. Geophys. Res.*, 108, 8473, <https://doi.org/10.1029/2002JD002226>, 2003.

391 Haywood, J. M., Abel, S. J., Barrett, P. A., Bellouin, N., Blyth, A., Bower, K. N., Brooks, M., Carslaw, K., Che, H.,  
392 Coe, H., Cotterell, M. I., Crawford, I., Cui, Z., Davies, N., Dingley, B., Field, P., Formenti, P., Gordon, H., de  
393 Graaf, M., Herbert, R., Johnson, B., Jones, A. C., Langridge, J. M., Malavelle, F., Partridge, D. G., Peers, F.,  
394 Redemann, J., Stier, P., Szpek, K., Taylor, J. W., Watson-Parris, D., Wood, R., Wu, H., and Zuidema, P.: The  
395 CLoud–Aerosol–Radiation Interaction and Forcing: Year 2017 (CLARIFY-2017) measurement campaign, *Atmos.*  
396 *Chem. Phys.*, 21, 1049–1084, <https://doi.org/10.5194/acp-21-1049-2021>, 2021.

397 Kacarab, M., Thornhill, K. L., Dobracki, A., Howell, S. G., O'Brien, J. R., Freitag, S., Poellot, M. R., Wood, R.,  
398 Zuidema, P., Redemann, J., and Nenes, A.: Biomass burning aerosol as a modulator of the droplet number in the  
399 southeast Atlantic region, *Atmos. Chem. Phys.*, 20, 3029–3040, <https://doi.org/10.5194/acp-20-3029-2020>, 2020.

400 Keil, A., and Haywood, J. M.: Solar radiative forcing by biomass burning aerosol particles during SAFARI 2000: A  
401 case study based on measured aerosol and cloud properties, *J. Geophys. Res. Atmos.*, 108, 8467,  
402 doi:10.1029/2002JD002315, 2003.

403 Klopper, D., Formenti, P., Namwoonde, A., Cazaunau, M., Chevaillier, S., Feron, A., Gaimoz, C., Hease, P., Lahmidi,  
404 F., Mirande-Bret, C., Triquet, S., Zeng, Z., and Piketh, S. J.: Chemical composition and source apportionment of  
405 atmospheric aerosols on the Namibian coast, *Atmos. Chem. Phys.*, 20, 15,811–15,833, doi:10.5194/acp-20-15811-  
406 2020, 2020.

407 Koch, D., and Del Genio A. D.: Black carbon semi-direct effects on cloud cover: review and synthesis, *Atmos. Chem.*  
408 *Phys.*, 10, 7685–7696, doi:10.5194/acp-10-7685-2010, 2010.

409 Lu, Z., Liu, X., Zhang, Z., Zhao, C., Meyer, K., Rajapakshe, C., Wu, C., Yang, Z., and Penner, J.: Biomass smoke  
410 from southern Africa can significantly enhance the brightness of stratocumulus over the southeastern Atlantic  
411 Ocean, *Proc. Natl. Acad. Sc.*, 115, 2924–2929, doi:10.1073/pnas.1713703115, 2018.

412 Mallet, M., Solmon, F., Nabat, P., Elguindi, N., Waquet, F., Bouniol, D., Sayer, A. M., Meyer, K., Roehrig, R.,  
413 Michou, M., Zuidema, P., Flaant, C., Redemann, J., and Formenti, P.: Direct and semi-direct radiative forcing of  
414 biomass-burning aerosols over the southeast Atlantic (SEA) and its sensitivity to absorbing properties: a regional  
415 climate modeling study, *Atmos. Chem. Phys.*, 20, 13191–13216, <https://doi.org/10.5194/acp-20-13191-2020>, 2020.

416 McFarquhar, G. M., and Wang, H.: Effects of aerosols on trade wind cumuli over the Indian Ocean: Model  
417 simulations, *Q. J. R. Meteorol. Soc.*, 132, 821–843, doi: 10.1256/qj.04.179, 2006.

418 Mechoso, C. R., Wood, R., Weller, R., Bretherton, C. S., Clarke, A. D., Coe, H., Fairall, C., Farrar, J. T., Feingold,  
419 G., Garreaud, R., Grados, C., McWilliams, J., de Szoeko, S. P., Yuter, S. E., and Zuidema, Z.: Ocean–cloud–  
420 atmosphere–land interactions in the Southeastern Pacific: The VOCALS program, *B. Am. Meteorol. Soc.*, 95, 357–  
421 375, doi:10.1175/BAMS-D-11-00246.1, 2013.

422 Meyer, K., Platnick, S., Oreopoulos, L., and Lee, D.: Estimating the direct radiative effect of absorbing aerosols  
423 overlying marine boundary layer clouds in the southeast Atlantic using MODIS and CALIOP, *J. Geophys. Res.*  
424 *Atmos.*, 118, 4801–4815, doi:10.1002/jgrd.50449, 2013.

425 Müller, D., Wandinger, U., and Ansmann, A.: Microphysical particle parameters from extinction and backscatter lidar  
426 data by inversion with regularization: theory, *Appl. Optics*, 38, 2346–2357, 1999a.

427 Müller, D., Wandinger, U., and Ansmann, A.: Microphysical particle parameters from extinction and backscatter lidar  
428 data by inversion with regularization: simulation, *Appl. Optics*, 38, 2358–2368, 1999b.

429 Müller, D., Hostetler, C. A., Ferrare, R. A., Burton, S. P., Chemyakin, E., Kolgotin, A., Hair, J. W., Cook, A. L.,  
430 Harper, D. B., Rogers, R. R., Hare, R. W., Cleckner, C. S., Obland, M. D., Tomlinson, J. Berg, L. K., and Schmid,  
431 B.: Airborne multiwavelength high spectral resolution lidar (HSRL-2) observations during TCAP 2012: vertical  
432 profiles of optical and microphysical properties of a smoke/urban haze plume over the northeastern coast of the US,  
433 *Atmos. Meas. Tech.*, 7, 3487–3496, doi:10.5194/amt-7-3487-2014, 2014.

434 Müller, D., Chemyakin, E., Kolgotin, A., Ferrare, R. A., Hostetler, C. A., and Romanov, A.: Automated, unsupervised,  
435 inversion of multiwavelength lidar data with TiARA: assessment of retrieval performance of microphysical  
436 parameters using simulated data, *Appl. Optics*, 58, 4981–5007, doi:10.1364/AO.58.004981, 2019.

437 Painemal, D., Kato, S., and Minnis, P.: Boundary layer regulation in the southeast Atlantic cloud microphysics during  
438 the biomass burning season as seen by the A-train satellite constellation, *J. Geophys. Res. Atmospheres*, 119,  
439 11,288–211,302, doi:10.1002/2014JD022182, 2014.

440 Peers, F., Francis, P., Fox, C., Abel, S. J., Szpek, K., Cotterell, M. I., Davies, N. W., Langridge, J. M., Meyer, K. G.,  
441 Platnick, S. E., and Haywood, J. M.: Observation of absorbing aerosols above clouds over the south-east Atlantic  
442 Ocean from the geostationary satellite SEVIRI – Part 1: Method description and sensitivity, *Atmos. Chem. Phys.*,  
443 19, 9595–9611, <https://doi.org/10.5194/acp-19-9595-2019>, 2019.

444 Penner, J. E., Zhang, S. Y., and Chuang, C. C.: Soot and smoke aerosol may not warm climate, *J. Geophys. Res.*  
445 *Atmospheres*, 108, 4657, doi:10.1029/2003JD003409, 2003.

446 Pistone, K., Zuidema, P., Wood, R., Diamind, M., da Silva, A. M., Ferrada, G., Saide, P. E., Ueyama, R., Ryoo, J.-  
447 M., Pfister, L., Podolske, J., Noone, D., Bennett, R., Stith, E., Carmichael, G., Redemann, J., Flynn, C., LeBlanc,  
448 S., Segal-Rozenhaimer, M., and Shinozuka, Y.: Exploring the elevated water vapor signal associated with the free  
449 tropospheric biomass burning plume over the southeast Atlantic Ocean, *Atmos. Chem. Phys.*, 21, 9643-9668,  
450 <https://doi.org/10.5194/acp-21-9643-2021>, 2021.

451 Pósfai, M., Simonics, R., Li, J., Hobbs, P. V., and Buseck, P. R.: Individual aerosol particles from biomass burning in  
452 southern Africa: 1. Compositions and size distributions of carbonaceous particles, *J. Geophys. Res.*, 108, 8483,  
453 doi:10.1029/2002JD002291, 2003.

454 Ramanathan, V., Crutzen, P. J., Kiehl, J. T., and Rosenfeld, D.: Aerosols, climate, and the hydrological cycle, *Science*,  
455 294(5549), 2119-2124, doi:10.1126/science.1064034, 2001.

456 Randles, C.A., daSilva, A. M., Buchard, V., Colarco, P. R., Darmenov, A., Govindaraju, P., Smirnov, A., Holben, B.,  
457 Ferrare, R. A., Hair, J., Shinozuka, Y., and Flynn, C. J.: The MERRA-2 aerosol reanalysis, 1980 onward. Part I:  
458 System description and data assimilation evaluation, *J. Climate*, 30, 6823–6850, doi: 10.1175/JCLI-D-16-0609.1,  
459 2017.

460 Redemann, J., Wood, R., Zuidema, P., Doherty, S. J., Luna, B., LeBlanc, S. E., Diamond, M. S., Shinozuka, Y., Chang,  
461 I. Y., Ueyama, R., Pfister, L., Ryoo, J.-M., Dobracki, A. N., da Silva, A. M., Longo, K. M., Kacencelenbogen, M.  
462 S., Flynn, C. J., Pistone, K., Knox, N. M., Piketh, S. J., Haywood, J. M., Formenti, P., Mallet, M., Stier, P.,  
463 Ackerman, A. S., Bauer, S. E., Fridlind, A. M., Carmichael, G. R., Saide, P. E., Ferrada, G. A., Howell, S. G.,  
464 Freitag, S., Cairns, B., Holben, B. N., Knobelspiesse, K. D., Tanelli, S., L'Ecuyer, T. S., Dzambo, A. M., Sy, O. O.,  
465 McFarquhar, G. M., Poellot, M. R., Gupta, S., O'Brien, J. R., Nenes, A., Kacarab, M., Wong, J. P. S., Small-  
466 Griswold, J. D., Thornhill, K. L., Noone, D., Podolske, J. R., Schmidt, K. S., Pilewskie, P., Chen, H., Cochrane, S.  
467 P., Sedlacek, A. J., Lang, T. J., Stith, E., Segal-Rozenhaimer, M., Ferrare, R. A., Burton, S. P., Hostetler, C. A.,  
468 Diner, D. J., Seidel, F. C., Platnick, S. E., Myers, J. S., Meyer, K. G., Spangenberg, D. A., Maring, H., and Guo, L.:  
469 An overview of the ORACLES (ObseRvations of Aerosols above Clouds and their intEractionS) project: aerosol-  
470 cloud-radiation interactions in the southeast Atlantic basin, *Atmos. Chem. Phys.*, 21, 1507-1563, doi:10.5194/acp-  
471 21-1507-2021, 2021.

472 Rogers, R. R., Hair, J. W., Hostetler, C. A., Ferrare, R. A., Obland, M. D., Cook, A. L., Harper, D. B., Burton, S. P.,  
473 Shinozuka, Y., McNaughton, C. S., Clarke, A. D., Redemann, J., Russell, P. B., Livingston, J. M., and Kleinman,  
474 L. I.: NASA LaRC airborne high spectral resolution lidar aerosol measurements during MILAGRO: observations  
475 and validation, *Atmos. Chem. Phys.*, 9, 4811-4826, 2009.

476 Ryoo, J.-M., Pfister, L., Ueyama, R., Zuidema, P., Wood, R., Chang, I., and Redemann, J.: A meteorological  
477 overview of the ORACLES (ObseRvations of Aerosols above Clouds and their intEractionS) campaign over the  
478 southeastern Atlantic during 2016–2018: Part 1 – Climatology, *Atmos. Chem. Phys.*, 21, 16689–16707,  
479 <https://doi.org/10.5194/acp-21-16689-2021>, 2021.

480 Sakaeda, N., Wood, R., and Rasch, P. J.: Direct and semidirect aerosol effects of southern African biomass burning  
481 aerosol, *J. Geophys. Res. Atmospheres*, 116, D12205, doi:10.1029/2010JD015540, 2011.

482 Sawamura, P., Moore, R. H., Burton, S. P., Chemyakin, E., Müller, D., Kolgotin, A., Ferrare, R. A., Hostetler, C. A.,  
483 Ziemba, L. D., Beyersdorf, A. J., and Anderson, B. E.: HSRL-2 aerosol optical measurements and microphysical  
484 retrievals vs. airborne in situ measurements during DISCOVER-AQ 2013: an intercomparison study, *Atmos. Chem.*  
485 *Phys.*, 17, 7229-7243, doi.org/10.5194/acp-17-7229-2017, 2017.

486 Schmid, B., Ferrare, R. A., Flynn, C., Elleman, R., Covert, D., Strawa, A., Welton, E., Turner, D., Jonsson, H.,  
487 Redemann, J., Eilers, J., Ricci, K., Hallar, A. G., Clayton, M., Michalsky, J., Smirnov, A., Holben, B., and Barnard,  
488 J. : How well do state-of-the-art techniques measuring the vertical profile of tropospheric aerosol extinction  
489 compare? *J. Geophys. Res.*, 111, D05S07, doi:10.1029/2005JD005837, 2006.

490 She, C. Y., Alvarez II, R. J., Caldwell, L. M., and Krueger, D. A.: High-spectral-resolution Rayleigh-Mie lidar  
491 measurement of aerosol and atmospheric profiles, *Opt. Lett.*, 17, 541-543, 1992.

492 Shingler, T., Crosbie, E., Ortega, A., Shiraiwa, M., Zuend, A., Beyersdorf, A., Ziemba, L., Anderson, B., Thornhill,  
493 L., Perring, A. E., Schwarz, J. P., Campazano-Jost, P., Day, D. A., Jimenez, J. L., Hair, J. W., Mikoviny, T.,  
494 Wisthaler, A., & Sorooshian, A.: Airborne characterization of subsaturated aerosol hygroscopicity and dry refractive  
495 index from the surface to 6.5km during the SEAC<sup>4</sup>RS campaign, *J. Geophys. Res.*, 121(8), 4188-4210,  
496 <https://doi.org/10.1002/2015JD024498>, 2016.

497 Shinozuka, Y., Saide, P. E., Ferrada, G. A., Burton, S. P., Ferrare, R. A., Doherty, S. J., Gordon, H., Longo, K., Mallet,  
498 M., Feng, Y., Wang, Q., Cheng, Y., Dobracki, A., Freitag, S., Howell, S. G., LeBlanc, S., Flynn, C., Segal-  
499 Rozenhaimer, M., Pistone, K., Podolske, J. R., Stith, E. J., Bennett, J. R., Carmichael, G. R., da Silva, A.,

500 Govindaraju, R., Leung, R., Zhang, Y., Pfister, L., Ryoo, J.-M., Redemann, J., Wood, R., and Zuidema, P.: Modeling  
 501 of the smoky troposphere of the southeast Atlantic: a comparison to ORACLES airborne observations from  
 502 September of 2016, *Atmos. Chem. Phys.*, 20, 11491-11526, doi:10.5194/acp-20-11491-2020, 2020.  
 503 Shipley, S. T., Tracy, D. H., Eloranta, E. W., Tauger, J. T., Stroga, J. T., Roesler, F. L., and Weinman, J. A.: High  
 504 spectral resolution lidar to measure optical scattering properties of atmospheric aerosols. 1. Theory and  
 505 instrumentation, *Appl. Optics*, 22, 3716-3724, 1983.  
 506 Stein, A.F., Draxler, R. R., Rolph, G. D., Stunder, B. J. B., Cohen, M. D., and Ngan, F.: NOAA's HYSPLIT  
 507 atmospheric transport and dispersion modeling system, *B. Am. Meteorol. Soc.*, 96, 2059-2077, doi:10.1175/BAMS-  
 508 D-14-00110.1, 2015.  
 509 Veselovskii, I., Kolgotin, A., Grazianov, V., Müller, D., Wandinger, U., and Whiteman, D. N.: Inversion with  
 510 regularization for the retrieval of tropospheric aerosol parameters from multi-wavelength lidar sounding, *Appl.*  
 511 *Optics*, 41, 3685-3699, 2002.  
 512 Wilcox, E. M.: Stratocumulus cloud thickening beneath layers of absorbing smoke aerosol, *Atmos. Chem. Phys.*, 10,  
 513 11769-11777, doi:10.5194/acp-10-11769-2010, 2010.  
 514 Wilcox, E. M.: Direct and semi-direct radiative forcing of smoke aerosols over clouds, *Atmos. Chem. Phys.*, 12, 139-  
 515 149, doi:10.5194/acp-12-139-2012, 2012.  
 516 Wu, H., Taylor, J. W., Szpek, K., Langridge, J. M., Williams, P. I., Flynn, M., Allan, J. D., Abel, S. J., Pitt, J., Cotterell,  
 517 M. I., Fox, C., Davies, N. W., Haywood, J., and Coe, H.: Vertical variability of the properties of highly aged biomass  
 518 burning aerosol transported over the southeast Atlantic during CLARIFY-2017, *Atmos. Chem. Phys.*, 20, 12697-  
 519 12719, <https://doi.org/10.5194/acp-20-12697-2020>, 2021.  
 520 Xu F., Gao, L., Redemann, J., Flynn C.J., Espinosa, W.R., da Silva, A.M., Stammes, S., Burton, S.P., Liu, X., Ferrare,  
 521 R., Cairns, B. and Dubovik, O.: A Combined Lidar-Polarimeter Inversion Approach for Aerosol Remote Sensing  
 522 Over Ocean, *Front. Remote Sens.*, 2:620871, doi: 10.3389/frsen.2021.620871, 2021.  
 523 Yamaguchi T, Feingold, G., Kazil, J., and McComiskey, A.: Stratocumulus to cumulus transition in the presence of  
 524 elevated smoke layers. *Geophys. Res. Lett.*, 42: 10478-10485, 2015.  
 525 Zhang, J. and Zuidema, P.: The diurnal cycle of the smoky marine boundary layer observed during August in the  
 526 remote southeast Atlantic, *Atmos. Chem. Phys.*, 19, 14493-14516, <https://doi.org/10.5194/acp-19-14493-2019>,  
 527 2019.  
 528 Zhang Z., Meyer, K., Yu, H., Platnick, S., Colarco, P. R., Liu, Z., and Oreopoulos, L.: Shortwave direct radiative  
 529 effects of above-cloud aerosols over global oceans derived from 8 years of CALIPSO and MODIS observations,  
 530 *Atmos. Chem. Phys.*, 16, 2877-2900, doi:10.5194/acp-16-2877-2016, 2016.  
 531 Zhang, X., Mao, M., Yin, Y., and Tang, S.: The absorption Ångström exponent of black carbon with brown coatings:  
 532 effects of aerosol microphysics and parameterization, *Atmos. Chem. Phys.*, 20, 9701-9711, doi:10.5194/acp-20-  
 533 9701-2020, 2020.  
 534 Zuidema, P., Redemann, J., Haywood, J., Wood, R., Piketh, S., Hipondoka, M., and Formenti, P.: Smoke and clouds  
 535 above the southeast Atlantic, *B. Am. Meteorol. Soc.*, 97, 1131-1135, doi:10.1175/BAMS-D-15-00082.1, 2016.  
 536 Zuidema, P., Sedlacek III, A. J. Flynn, C., Springston, S., Delgado, R., Zhang, J., Aiken, A. C., Koontz, A., and  
 537 Muradyan, P.: The Ascension Island boundary layer in the remote Southeast Atlantic is often smoky, *Geophys. Res.*  
 538 *Lett.*, 45, 4456-4465, doi:10.1002/2017/GL076926, 2018.  
 539

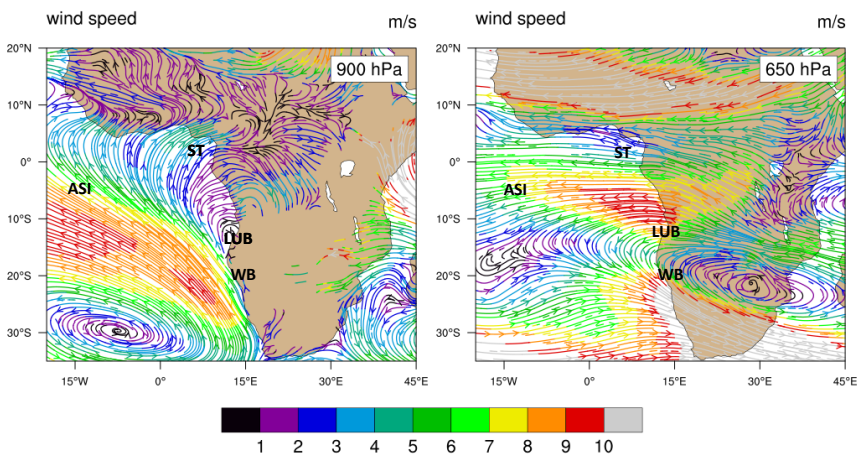
540  
541  
542

**Table 1:** Averaging area, flight time periods, the duration over water and number of HYSPLIT backward trajectories, and number of HSRL-2 profiles in each grid box used in the study.

Box	Averaging Area	Averaging Days	Time of Day	Duration in Hours Over Water at 3.5 km	Number of Profiles
A	11° S-9° S; 1° W-1° E	9/12,16	11:00 UTC	44.3±7.0 (N = 19)	50
B	10° S-8° S; 8° E-10° E	9/12,16,18	10:00 UTC	14.9±4.5 (N = 27)	56
C	16° S-14° S; 4° E-6° E	9/12,16	13:00 UTC	40.4±7.2 (N = 19)	51
D	14° S-12° S; 10° E-12° E	9/18,24	09:00 UTC	5.5±2.0 (N = 27)	46
E	23° S-21° S; 8° E-10° E	9/20,22	14:00 UTC	-	36

543

544



545  
546  
547  
548  
549  
550

**Figure 1:** MERRA2 monthly mean reanalysis of 900 and 650 hPa streamlines for September 2016. Stations marked are Ascension Island (ASI), Lubango (LUB), a long-term AERONET site at 2 km elevation, and Walvis Bay (WB), where ER-2 flights originated from during the September 2016 ORACLES IOP. Flights in August 2017 and September/October 2018 originated from São Tomé (ST).



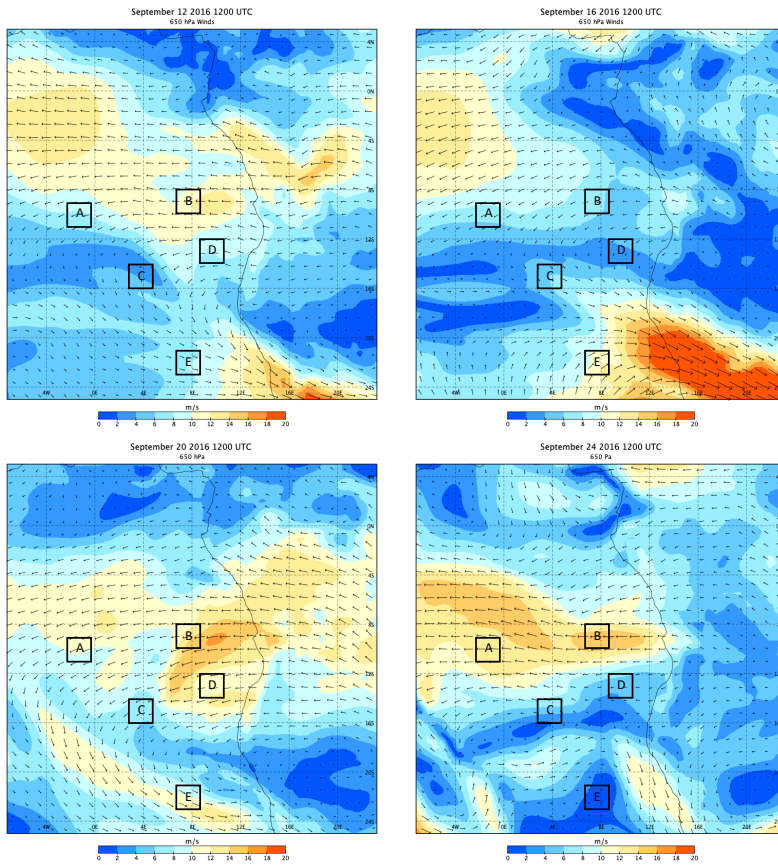
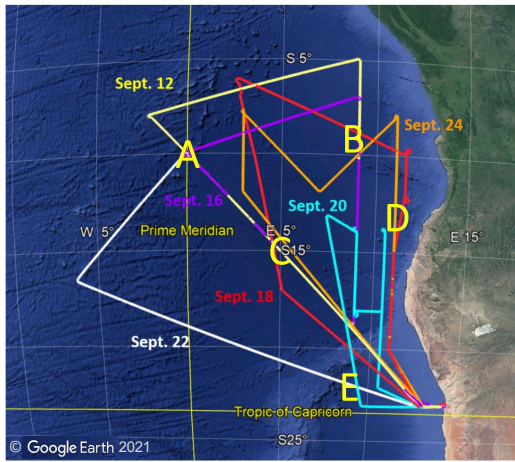


**Figure 2:** MERRA2 reanalysis of 650 hPa winds at 1200 UTC on September 12, 16, 20, 24, 2016. Grid boxes in the study are marked with letters.

551  
552  
553  
554

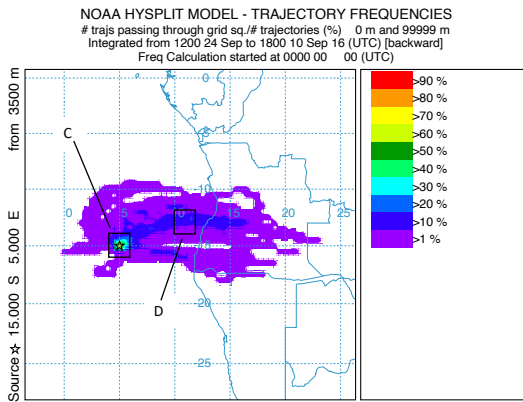
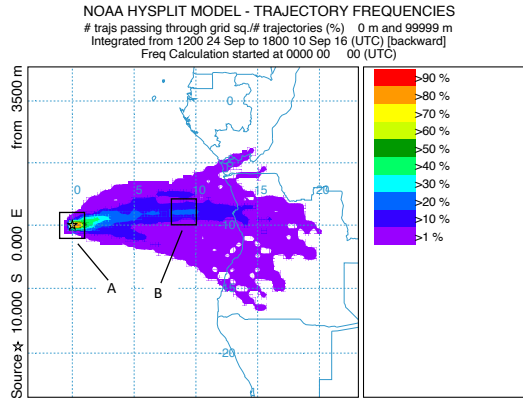
555  
556



557  
558  
559  
560  
561

**Figure 3:** HSRL-2 science data flight tracks during the September 2016 IOP. Letters refer. to the grid boxes identified in Fig. 2

562



563  
564  
565  
566  
567  
568

**Figure 4:** Frequency distribution of 48-hour backward trajectories of air parcels arriving at 3500 m above the centers of grid boxes A and C over the time period of the campaign. Grid boxes B and D are upstream of grid boxes A and C, respectively.

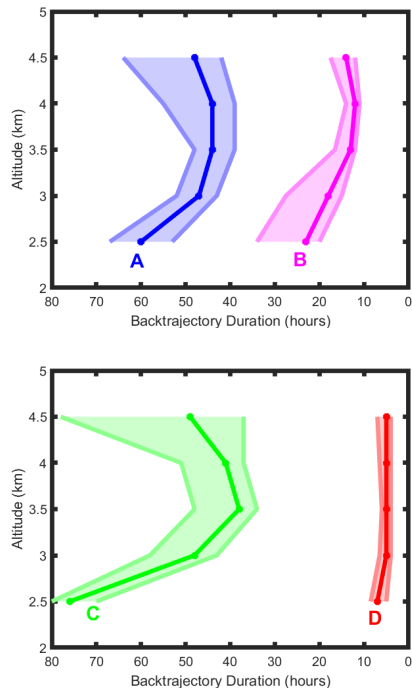
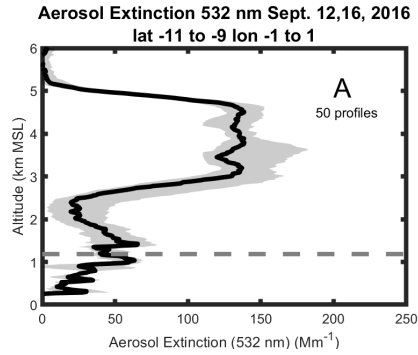


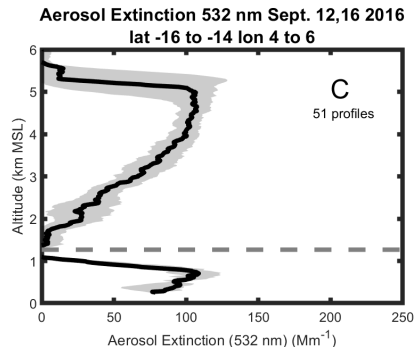
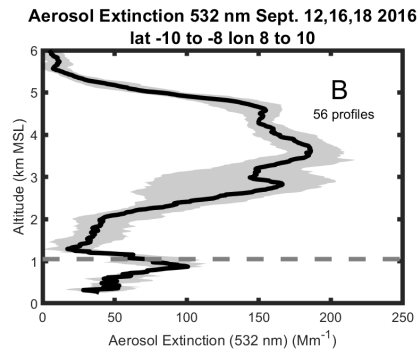
**Figure 5:** Duration of time spent over water of air parcels arriving at grid boxes marked on the figure. Solid lines are median values, and the shaded portion are the range of the 75<sup>th</sup> and 25<sup>th</sup> percentile. The number of trajectories used for the calculation are in Table 1. Trajectory hours are shown in reverse to correspond to the map in Fig. 4.

570  
 571  
 572  
 573  
 574  
 575  
 576

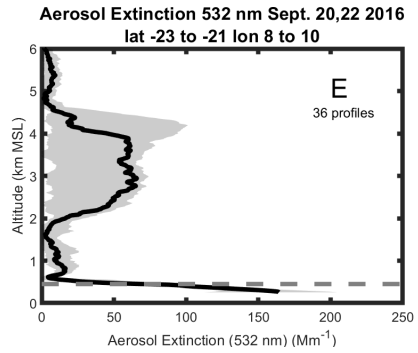
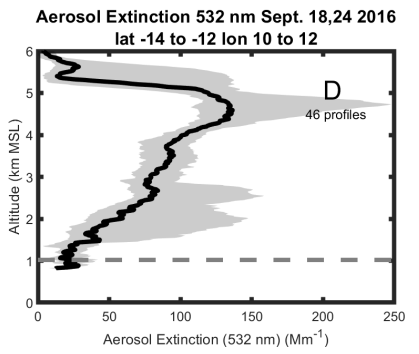
577



578



579



580

581

582

583

584

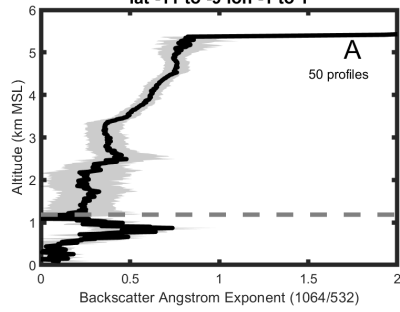
585

586

**Figure 6:** Average vertical profiles of the aerosol extinction coefficient at 532 nm in grid boxes A (upper left), B (upper right), C (middle left), D (middle right) and E (lower left). The averaging area, dates of flights and total number of one-minute profiles are also shown. The dark line represents the median value and grey shades contain the 25<sup>th</sup> to 75<sup>th</sup> percentiles. Dashed line refers to the mean cloud top height.

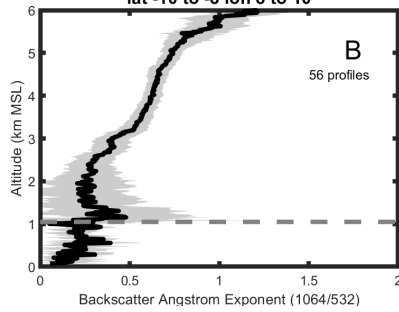
587

**Backscatter Ang. Expo. 1064/532 Sept. 12,16, 2016**  
**lat -11 to -9 lon -1 to 1**

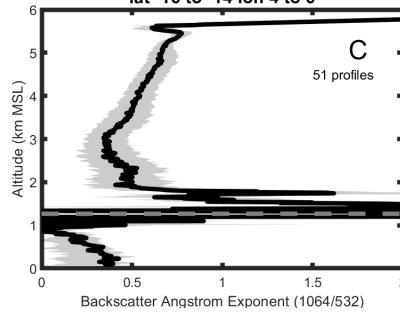


588

**Backscatter Ang. Expo. 1064/532 Sept. 12,16,18 2016**  
**lat -10 to -8 lon 8 to 10**

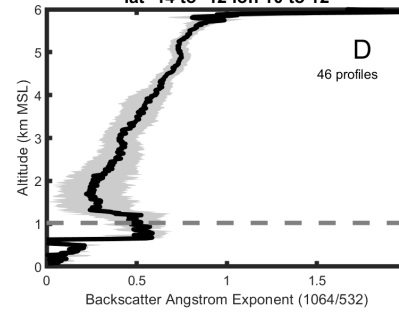


**Backscatter Ang. Expo. 1064/532 Sept. 12,16 2016**  
**lat -16 to -14 lon 4 to 6**

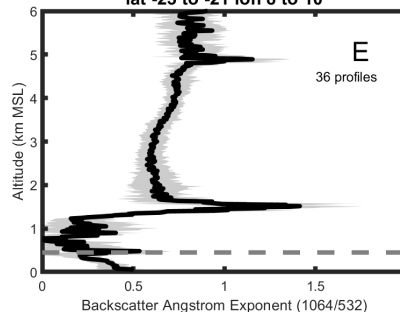


589

**Backscatter Ang. Expo. 1064/532 Sept. 18,24 2016**  
**lat -14 to -12 lon 10 to 12**



**Backscatter Ang. Expo. 1064/532 Sept. 20,22 2016**  
**lat -23 to -21 lon 8 to 10**



590

591

592

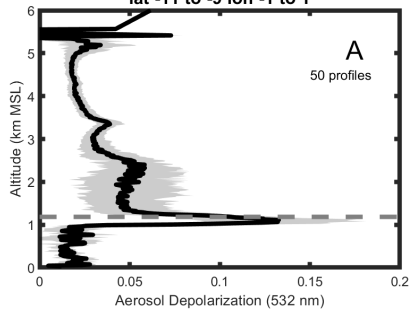
593

594

**Figure 7:** As in Fig. 6 but for the Wavelength Dependent Backscatter Ångström exponent between 1064 and 532 nm.

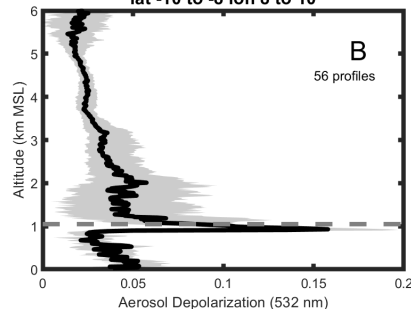
595

**Aerosol Depolarization 532 nm Sept. 12,16, 2016  
lat -11 to -9 lon -1 to 1**

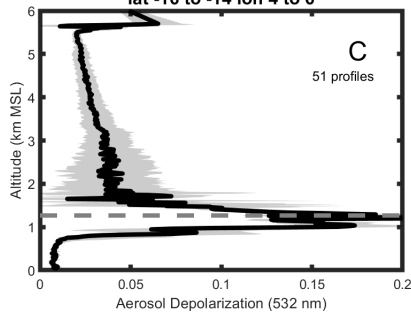


596

**Aerosol Depolarization 532 nm Sept. 12,16,18 2016  
lat -10 to -8 lon 8 to 10**

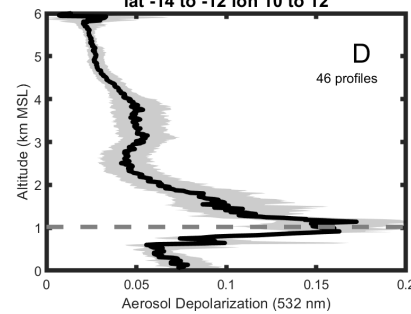


**Aerosol Depolarization 532 nm Sept. 12,16 2016  
lat -16 to -14 lon 4 to 6**

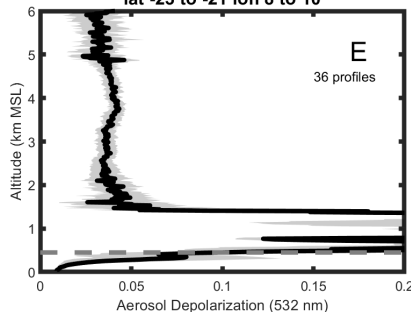


597

**Aerosol Depolarization 532 nm Sept. 18,24 2016  
lat -14 to -12 lon 10 to 12**



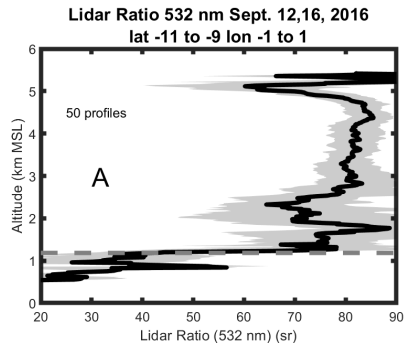
**Aerosol Depolarization 532 nm Sept. 20,22 2016  
lat -23 to -21 lon 8 to 10**



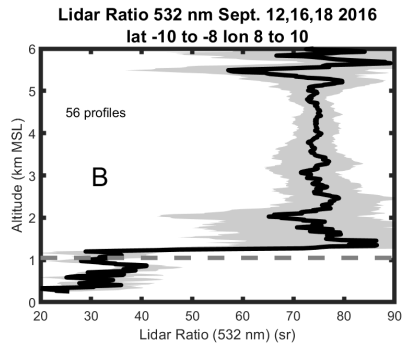
598  
599  
600  
601

**Figure 8:** As in Fig. 6 but for the aerosol depolarization at 532 nm.

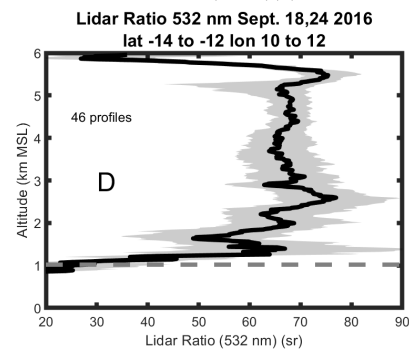
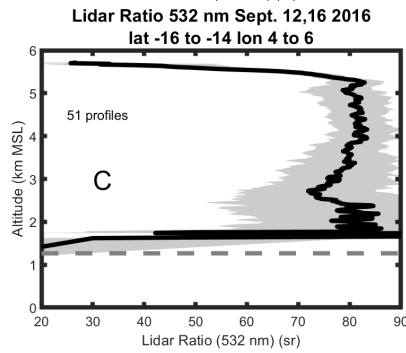
602



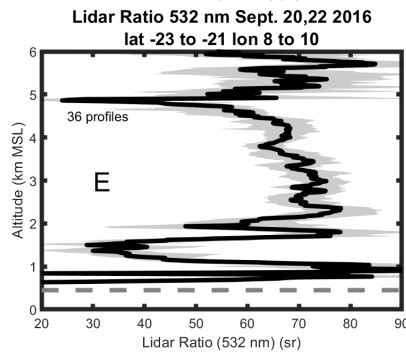
603



604



605



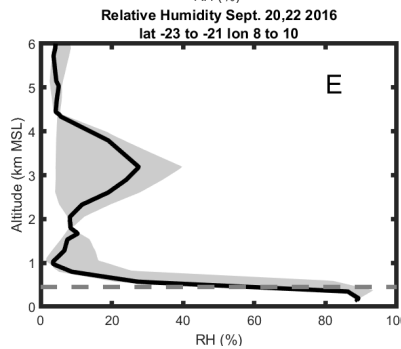
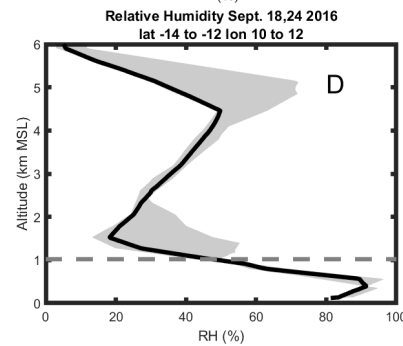
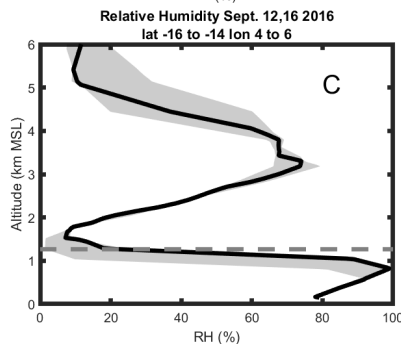
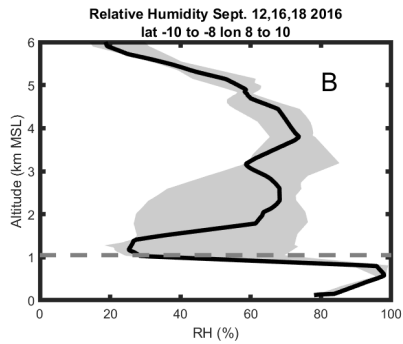
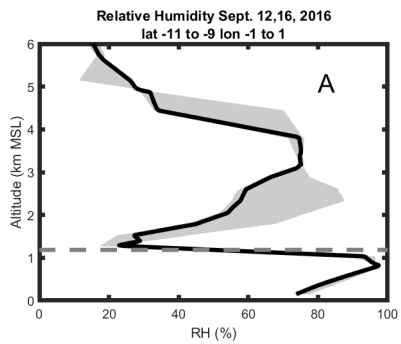
606

**Figure 9:** As in Fig. 6 but for the Lidar Ratio at 532 nm.

607

608



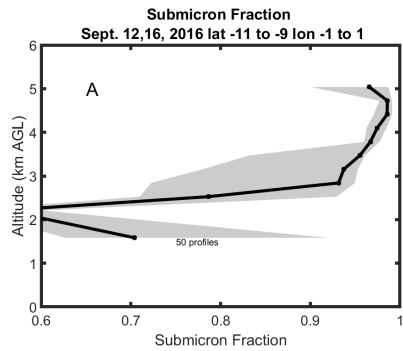


609

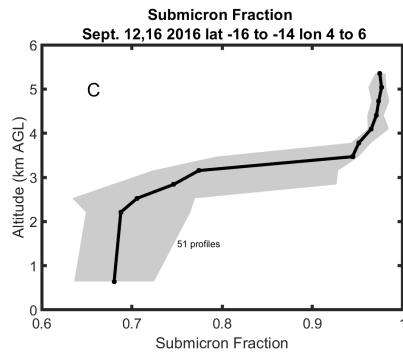
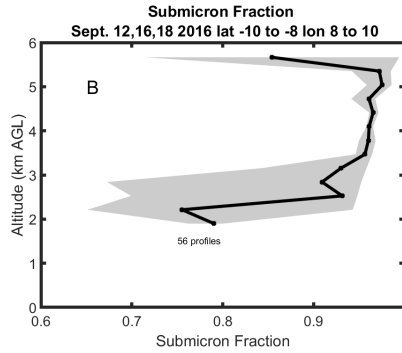
610

611  
612  
613  
614  
615  
616  
617  
618

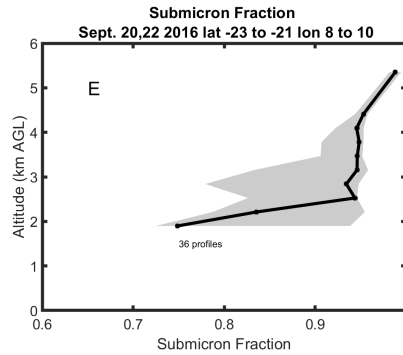
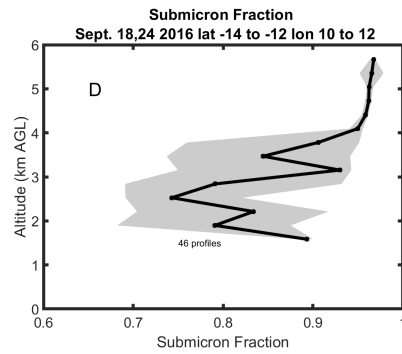
**Figure 10:** Relative Humidity (%) in grid boxes A (upper left), B (upper right), C (middle left), D (middle right) and E (lower left) from MERRA2 reanalysis corresponding to the HSRL-2 profiles shown in Figs. 6-9. The dark line represents the median value and grey shades contain the 25<sup>th</sup> to 75<sup>th</sup> percentiles. Dashed line refers to the mean cloud top height.



619



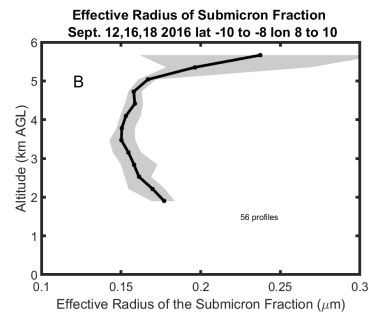
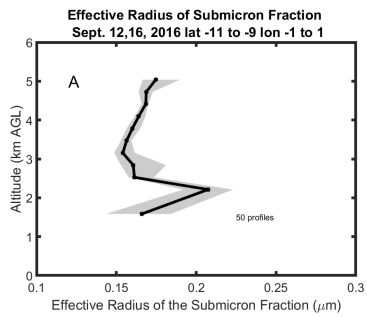
620



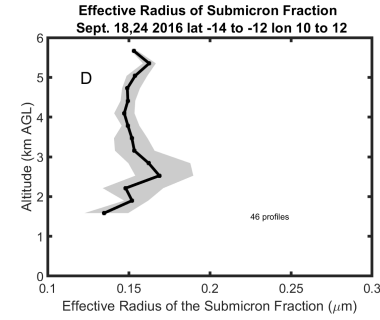
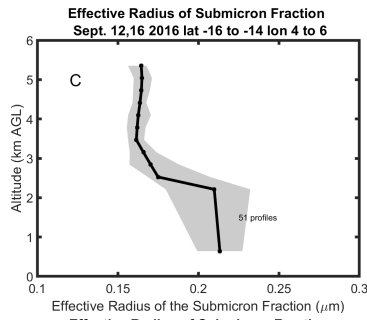
621  
622  
623  
624  
625  
626  
627

**Figure 11:** Average vertical profiles of the submicron fraction in grid boxes A (upper left), B (upper right), C (middle left), D (middle right) and E (lower left). The averaging area, dates of flights and total number of one-minute profiles in the average are also shown. The dark line represents the median value and grey shades contain the 25<sup>th</sup> to 75<sup>th</sup> percentiles.

628



629



630  
631  
632

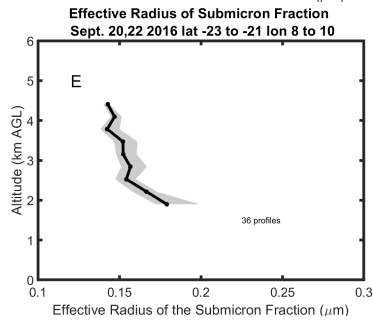


**Figure 12:** As in Fig. 11 but for the effective radius of the submicron fraction.